Research Article | Vol. 26, No. 23 | 12 Nov 2018 | OPTICS EXPRESS 30862
Optics EXPRESS

Significantly enhanced infrared absorption of graphene photodetector under surface-plasmonic coupling and polariton interference

YE ZHANG,[1] DEJIA MENG,[2] XIAO LI,[1] HONGHAO YU,[1] JIANJUN LAI,[1] ZHAOYANG FAN,[3] AND CHANGHONG CHEN[1,*]

[1]*Wuhan National Laboratory for Optoelectronics, Huazhong University of Science and Technology, Wuhan 430074, China*
[2]*State Key Laboratory of Applied Optics, Changchun Institute of Optics, Fine Mechanics and Physics, Chinese Academy of Science, Changchun 130033, China*
[3]*Nano Tech Center and Department of Electrical and Computer Engineering, Texas Tech University, Lubbock, TX 79409-3102, USA*
ch_chen@hust.edu.cn

Abstract: Here, we present a graphene-based long-wavelength infrared photodetector, for enhancing the infrared absorption of which the design consists of magnetic- and electric-plasmon resonators of metasurface to excite the graphene surface-plasmonic polaritons (SPPs). Through tuning the graphene Fermi energy to achieve the distinct resonances in a matching frequency, peak graphene absorbance exceeding 67.2% is confirmed, even when a lossy dielectric is used, and the field angle of view is up to 90°. If the graphene is of a different carrier mobility, then the absorption frequency is lockable, and the device always can keep the system absorbance close to 100 percent. The significantly enhanced graphene absorbance, up to ~29-fold that of a suspended graphene (general 2.3%), is attributed to the surface-plasmonic coupling between the magnetic and the electric resonances, as well as Fabry-Pérot interference of the coherent SPPs. The plasmonic cavity-mode model and equivalent-circuit method developed in this study will also be useful in guiding other optoelectronic device design.

1. Introduction

Graphene, a two-dimensional semiconductor with zero bandgap, has many intriguing properties [1–4]. With its high carrier mobility, the material shows great promise for applications in high-speed transistors and sensitive photodetectors. For the latter, high optical absorption of the graphene or the system of device is always desired. The opacity of a suspended graphene is determined solely by the fine structure constant, $\alpha = e^2/\hbar c$ (where e is the electron charge, $\hbar$ the reduced Planck's constant, and c the speed of light in vacuum). Its unique conical electronic band structure results in a constant absorbance of ~2.3%, $A_G' = \pi\alpha$, for normal incidence of electromagnetic (EM) waves over a broad frequency range from ultraviolet to infrared regime [5]. Such an absorbance is significant for only one-atomic thickness of graphene; however, it is insufficient for a practical photodetector. The low absorption limits its photoelectric responsivity, while the lack of spectral selectivity potentially is another problem for selective detection.

Since surface plasmons (SPs) or surface-plasmonic polaritons (SPPs) in shorter wavelength than incident light (λ_0) are capable of stronger near-field localization or much tighter spatial confinement, the SP technology has rapidly emerged as an effective tool to pursue extreme light-matter interactions. Graphene SPs, the collective oscillations of charge carriers in extrinsic graphene, are available through intraband transitions excited by the optical field of infrared radiation. Comparing with noble metals, graphene has the highly tunable real part and much smaller imaginary part of permittivity [6–8]. Recently, the

#346679 https://doi.org/10.1364/OE.26.030862
Journal © 2018 Received 24 Sep 2018; revised 27 Oct 2018; accepted 4 Nov 2018; published 8 Nov 2018

Optics EXPRESS

methods to manipulate the graphene SPs by tuning the permittivity have attracted much attention [9–12]. As one of the metasurfaces, the structure of graphene integrated with subwavelength gold gratings was used to activate the graphene SPs directly by electric-field-driven LC (inductor-capacitor) resonances (electric SPs) [13]. Magnetic-field-induced LC resonances (magnetic SPs) occur in similar structures, where the graphene SPs or SPPs are ascribed to a strong EM coupling from the magnetic SPs of the metals. The graphene absorbance at λ_0 = 9.09 μm was boosted to 72% for a hybrid-SP system with zero dielectric loss [14], and multi-band perfect absorption was demonstrated for another system [15]. On the contrary, the graphene SPs generally are not activated in the spectral range from ultraviolet to near infrared. Owing to larger absorption coefficient from interband transitions in combination with strongly localized field from magnetic SPs of the metals, the optical absorption of graphene will be much higher, and those pure metallic-SP structures show great potential for the applications of perfect absorbers [16–21] and metal-insulator-metal (MIM) waveguide [22]. Furthermore, the magnetic-SP structure tolerates a wide range of spatial incident angle [23]. With these progresses, achieving the graphene SP coupling and absorption enhancement in long-wavelength infrared (LWIR) remains a great challenge for graphene-based optoelectronics, especially photodetector [24–27], where the graphene absorption is dominated by the intraband transitions.

In this article, we present a tunable graphene-based LWIR photodetector design using metasurface structure, which can dramatically enhance the optical absorption. The design is based on the EM-coupling effect between two distinct resonance elements of magnetic and electric SPs and the standing-wave effect of coherent SPPs in Fabry-Pérot (F-P) cavity modes. It is found that by tuning the graphene Fermi energy (E_F) to achieve the frequency matching for the electric and the magnetic SPs, EM-wave scattering is suppressed, while the infrared absorption of the graphene, even in different carrier mobility, is significantly enhanced at the fixed frequency. The underlying mechanisms revealed here will be helpful in guiding the design of high-performance graphene photodetector, and perhaps also be relevant to the design of other optoelectronic devices.

2. Device and method

Figure 1 illustrates the schematic metasurface structure of designed graphene LWIR photodetector. It consists of top-metal pattern, single layer of graphene, low-loss insulator layer of Al_2O_3, and bottom-metal film. The top-metal pattern works as subwavelength shallow gratings and interdigital electrodes. The graphene sheet acts as the photosensitive semiconductor. The insulator layer is the dielectric to compose the micro capacitor in LC resonators. The bottom-metal film takes a role as the optical reflector and also as the back-gated electrode. When worked as the source/drain electrodes, the interdigitated grating has spectral selectivity and also contributes to high photoconductive gain. The dielectric layer interposes between the bottom metal and the grated graphene. This arrangement is used to build MIM and metal-insulator-semiconductor (MIS) configurations. Under TM-polarized infrared illumination, the MIM configuration constitutes arrayed magnetic-SP resonators. On the contrary, if the bottom metal is excluded, the graphene sheet conducting with the gratings forms a simple electric-SP resonator array. Two types of the resonator arrays are embedded together to enhance the graphene SPPs (if supported) through strong SP coupling. Moreover, if F-P interference condition of the SPPs is satisfied between the two neighboring gratings (slotted section), the coherent SPPs in cavity modes will confine more EM energies at the Air/Graphene/Al_2O_3 interfaces within the grating slots. As another function, the MIS configuration is used to electrostatically tune the graphene Fermi energy by the gate field.

Optical reflection of the device system is simulated by the method of finite differential time domain (FDTD solutions 8.15, Lumerical). In simulation, the TM-polarized infrared radiation of $|\boldsymbol{E}_0|$ = 1.0 V/m is always considered at normal incidence (along the y axis), except for determining the field angle of view (θ_{FV}). The polycrystalline dielectric film of Al_2O_3 is

Optics EXPRESS

assumed to be isotropic, and the permittivity (ε_D) values in Ref [28] are used. The graphene is an anisotropic material with in-plane permittivity, $\varepsilon_G = 1 + i\sigma/(\omega\varepsilon_0\Delta)$, and out-of-plane permittivity $\varepsilon_\perp = 2.5$ [29], where ω is the radiation angle frequency ($f = \omega/2\pi$ is frequency), σ and Δ are the optical conductivity and the thickness of graphene, respectively, and ε_0 is the vacuum permittivity. The conductivity used here is the calculated results from the Kubo formula, and it is attributed to intraband transitions in extrinsic graphene (E_F>77.5 meV) under the LWIR illumination. Then, the conductivity can be written as [30]:

$$\sigma(\omega) = i\frac{2e^2 k_B T}{\pi\hbar^2\left(\omega + i\tau^{-1}\right)}\ln\left[2\cosh\left(\frac{E_F}{2k_B T}\right)\right], \tag{1}$$

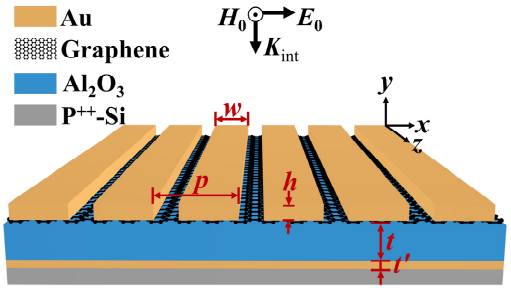

Fig. 1. Schematic structure of the graphene-based photodetector under normal incidence of TM-polarized radiation: incident electric field ($\boldsymbol{E}_0$), magnetic field ($\boldsymbol{H}_0$), and longitudinal wave vector ($\boldsymbol{K}_{int}$) in a coordinate system. Structural parameters: grating period (p), width (w), and height (h); Al_2O_3 dielectric thickness (t); bottom metal thickness (t'). h = 100 nm is selected for the height larger than EM-wave penetration depths (δ_M), t = 300 nm for nearly t-independence of the electric-SP frequency ($f_{SP,e}$), and t' = 200 nm for near-zero transmission. For the magnetic SPs, EM dissipation in the low-loss dielectric increases with the dielectric thickness, and the graphene absorption is thus reduced. The selected thickness is a compromise with the low dielectric loss.

where k_B is Boltzmann's constant, T is temperature, and $\tau = \mu E_F/(e v_F^2)$ is the relaxation time of carrier. The absorption spectra are obtained on the assumptions of T = 300 K, the Fermi velocity $v_F \approx 10^6$ m/s, and the carrier mobility $\mu \approx 2 \times 10^3$ $cm^2V^{-1}s^{-1}$ [30]. On a case by case basis, we also consider the absorption spectra to change with the mobility. The optical absorbance of graphene is calculated by the equation [17]:

$$A_G = \frac{2\pi}{\lambda_0 |E_0|^2 S}\varepsilon_G''\iiint_V |E_G|^2\, dV. \tag{2}$$

Here, V is the graphene volume, $\boldsymbol{E}_G$ is the local electric field in the graphene, and S is the irradiated area of the device system.

3. Results and discussion

Magnetic and electric SPs can be discriminated by the distributions of field and surface current density in resonance. Distinct from the electric SPs, the magnetic SPs are generally observed for the MIM configuration, where anti-parallel currents are sustained in the two layers of metal to produce an induced magnetic field confined mainly in the dielectric spacer.

Figure 2 shows the equivalent circuits and the distributions of surface current density; here, the illustrated electric SPs are the 4th-order (n = 4) mode along the Air/Graphene/Al_2O_3 interfaces. The different grating parameters, (p, w) = (3.0, 1.0) and (7.0, 5.0) (hereinafter in μm), are selected to detune the magnetic-SP frequency ($f_{SP,m}$) off the electric one ($f_{SP,e}$). Note that the different gratings turn out to be in an identical slot width (w'_G), *i.e.*, (p-w) = 2.0 μm. The following results of equivalent circuit analysis verify that $f_{SP,e}$ is independent of w, and in

Optics EXPRESS

both cases it corresponds to the free-space wavelengths of $\lambda_{0,e}$ = 10.15 μm. Generally, $f_{SP,m}$ is inversely proportional to w [31]. We find that for the structure of (p, w) = (7.0, 5.0), fundamental magnetic SPs in dipole mode also locates at $\lambda_{0,m}$≈10.15 μm, well matched with the electric SPs; while for (p, w) = (3.0, 1.0), the magnetic-SPs shift out from LWIR spectral range. As shown in Fig. 2(a), the current densities for the magnetic and the electric SPs, both at $\lambda_{0,e}$;$\lambda_{0,m}$ = 10.15 μm, are obviously to be high. Maximum current densities along the x axis are extracted to be $J_{x,G}$ = 7.77 × 10^6 A/m^2, distributed in the slotted graphene, and $J_{x,M}$ = 5.72 × 10^5 A/m^2 on the bottom metal. In contrast, we observe that $J_{x,G}$ significantly decreases with large detuning of $f_{SP,m}$ and $f_{SP,e}$. If the graphene is removed, only the magnetic-SP mode is retained with its location shifted to $\lambda_{0,m}$ = 10.32 μm, and $J_{x,M}$ increases to 1.27 × 10^6 A/m^2. The red-shift of $f_{SP,m}$ results from change of the equivalent circuit in the absence of graphene. On the contrary, only the electric-SP mode at $\lambda_{0,e}$ = 10.15 μm is observable for (p, w) = (3.0, 1.0), as shown in Fig. 2(b), and $J_{x,G}$ decreases to 1.03 × 10^6 A/m^2 as $\lambda_{0,m}$ is detuned off. The changes of $J_{x,G}$ and $J_{x,M}$ confirm a strong EM-coupling effect occurred between the magnetic and the electric SPs. Excluding the effect of grating fill-factor, we estimate that ~24.4-fold EM energy ($\Phi \propto J_{x,G}^2$) is further confined in the graphene by the electric- and magnetic-SP coupling.

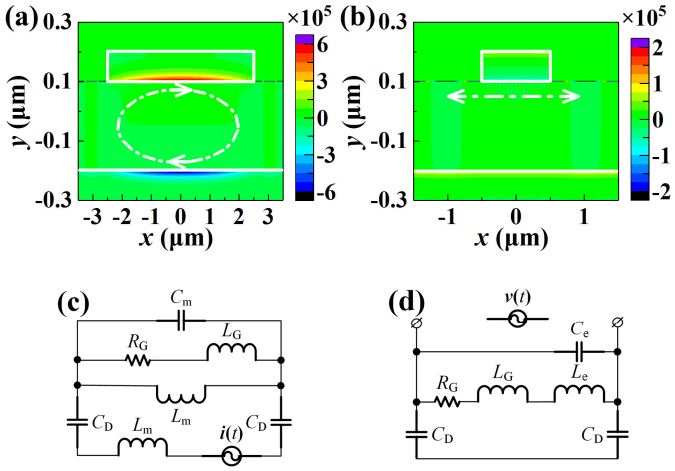

Fig. 2. When E_F = 0.6 eV, distributions of surface current density at: (a) $\lambda_{0,m}$;$\lambda_{0,e}$ = 10.15 μm for the structure of (p, w) = (7.0, 5.0) with the magnetic- and electric-SP modes both involved; (b) $\lambda_{0,e}$ = 10.15 μm for (p, w) = (3.0, 1.0), where $f_{SP,m}$ is detuned. Color bar: $J_{x,G(M)}$ in A/m^2; to guide the eyes, the boundaries of grating and bottom metal (in white solid line) are highlighted. RLC equivalent circuits: (c) the magnetic SPs in dipole mode for (p, w) = (7.0, 5.0); (d): the electric SPs in n^{th}-order mode for (p, w) = (3.0, 1.0), of which the bottom-metal inductance (L_e') is negligible if the dielectric is thick enough to satisfy $(\omega C_D)^{-1} >> \omega L_e'$.

To understand the underlying mechanism of absorption enhancement, an equivalent circuit model is used to interpret the EM-coupling effect between the magnetic and the electric SPs. First of all, for the electric-field response, the graphene or the metals with negative $\varepsilon'_{G(M)}$ is equivalent to a series connection of resistor and self-inductor, and the resistance (R_G or R_M) and the inductance ($L_{e,G}$ or $L_{e,M}$) are given by [32,33]:

$$R_{G(M)} + i\omega L_{e,G(M)} = \gamma_1 \frac{w'_{G(M)}}{\varepsilon_0 \omega l \delta_{G(M)}} \left(\frac{\varepsilon''_{G(M)}}{\varepsilon'^2_{G(M)} + \varepsilon''^2_{G(M)}} - \frac{i\varepsilon'_{G(M)}}{\varepsilon'^2_{G(M)} + \varepsilon''^2_{G(M)}} \right), \quad (3)$$

where γ_1 = 0.2 or 1.0 (fitting values) is a coefficient to calculate the effective cross section of surface current for the graphene or the metals, w'_M and l are width ($w'_M = w$) and length of the

Optics EXPRESS

gratings along the x and z axes, respectively, and $\varepsilon_{G(M)} = \varepsilon'_{G(M)} + i\varepsilon''_{G(M)}$ is the complex permittivity of graphene or the metals. The EM-wave penetration depth is $\delta_G = \Delta$, for the graphene, or $\delta_M = \lambda_0/[4\pi \mathrm{Im}(\varepsilon_M^{1/2})]$ for the metal; obviously, $\delta_G << \delta_M$. In the spectral region of interest, $R_G >> R_M$ and $L_{e,G} >> L_{e,M}$ can be derived if w'_G is close to w'_M. Hence, R_M and $L_{e,M}$ are negligible, and $f_{SP,e}$ is thus independent of w'_M. Secondly, the arrayed MIM configuration exhibits both inductive and capacitive behavior when it responds to the transversal magnetic field. The inductance (L_m) is a sum of self-inductance ($L_{e,M}$) and mutual inductance ($L_{m,M}$) of the metals, *i.e.*, $L_m = L_{e,M} + L_{m,M}$. Approximately, $L_{m,M} = 0.5\mu_0 wt/l$, where μ_0 is vacuum permeability. The capacitance from the dielectric contribution is written as parallel-plated capacitor formula, $C_D = \gamma_2 \varepsilon_0 \varepsilon_D wl/t$, where $\gamma_2 = 0.222$ is an effective area coefficient for uneven electric-field distribution in the dielectric [34].

Figures 2(c) and 2(d) illustrate the RLC circuits for responses to the externally electric and magnetic fields of radiation, respectively. Here, $L_e = L_{e,M}$ and $L_G = L_{e,G}$. In the case $l >> w'_G >> h$, the parallel-wired capacitance to the magnetic response that accounts for the slotted-air contribution can be expressed as $C_m = \pi\varepsilon_0 l/\ln(w'_G/h)$; while the electric-response capacitance of the slotted graphene, C_e, is mode-dependent, and can be determined by the grating structure and an effective permittivity of the interfaces. Therefore, the fundamental frequency of magnetic SPs is written as:

$$f_{SP,m} = \frac{1}{2\pi}\left[\left(\frac{1}{L_m}+\frac{1}{2L_G}\right)\frac{1}{C_m}+\frac{1}{L_m C_D}-\frac{\sqrt{-8L_m^2 L_G (L_m+L_G)C_m C_D + \left(L_m^2 C_D + 2L_m L_G C_m + 2L_m L_G C_D\right)^2}}{2L_m^2 L_G C_m C_D}\right]^{-\frac{1}{2}}. \quad (4)$$

Assuming L_m is close to L_G and $C_D >> C_m$, this frequency approaches to $f_{SP,m} = 0$, suggesting that the magnetic SPs are no longer supported. For the electric SPs, only the even-order modes can be excited by the radiation, and the mode-dependent frequency is:

$$f_{SP,e} = \frac{1}{2\pi}\left[(L_G + L_e)\left(C_e + \frac{C_D}{2}\right)\right]^{-\frac{1}{2}}. \quad (5)$$

From Eq. (5), $f_{SP,e}$ is certain to be w-independent in the case $L_e << L_G$, and nearly keeps unchanged for different dielectric thickness when the dielectric is thick enough to satisfy $C_D << C_e$, too.

If $f = f_{SP,e}$ or $f = f_{SP,m}$, more EM-radiation energies are absorbed by the intraband transitions of graphene after coupled to the graphene SPs and confined at the Air/Graphene/Al_2O_3 interfaces; otherwise, the energy of graphene SPs is attenuated due to non-zero imaginary impedance of the RLC circuit. Furthermore, when the electric and the magnetic SPs are matched in frequency, the absorption can reach a maximum at $f = f_{SP,e} = f_{SP,m}$.

Both the grating parameters and the graphene Fermi energy decide the electric-SP frequency, while the magnetic-SP frequency is dominated only by the grating parameters. Thus, an appropriate grating structure in combination with the tunable E_F can be used to guarantee $f_{SP,m}$ and $f_{SP,e}$ matching. In reality, $f_{SP,m}$ can be exactly calculated, and the magnetic SPs in fundamental mode can lead to lower EM dissipations than higher-order modes when the frequency keeps unchanged; instead, $f_{SP,e}$ can be located on the basis of the following F-P model of SPPs, owing to an uncertain value of C_e when the electric SPs are in higher-order modes. Figures 3(a) and 3(b) illustrate the magnetic-SP frequency dependence of the grating structure. It is confirmed that for a fixed period of p = 7.0 μm, $\lambda_{0,m}$ blue-shifts from 10.47 to 8.99 μm as the grating width decreases from w = 6.0 to 3.0 μm; while for a fixed grating width of w = 5.0 μm, the magnetic SPs keep the wavelength at $\lambda_{0,m}$ = 10.23 μm nearly unchanged when the period is varied. $f_{SP,m}$ is off proportional to $1/w$, but does not depend on p to a large extent [35]. It is observed that $\lambda_{0,m}$ calculated from Eq. (4) are in good agreement

Optics EXPRESS

with the simulated. Figure 3(c) shows the graphene absorption spectra at different E_F when the magnetic-SP frequencies are detuned. Indeed, only the even-order electric SPs are observable. For each order of the electric-SP modes, $\lambda_{0,e}$ is blue-shifted and the graphene absorbance increases with the Fermi energy. In LWIR spectral region, $|\varepsilon'_G|$ increases but ε''_G decreases with the increased E_F when E_F>77.5 meV. As a consequence of Eq. (3), the equivalent impedances, R_G and ωL_G, decrease, leading to the decreasing $\lambda_{0,e}$. However, the increasing graphene absorption is still insufficient for a practical device if only electric SPs are involved. Figure 3(d) shows how the spectra in absorbance change with the involvement of magnetic-SPs. With a constant slot width, all electric SPs in the same mode have nearly the same frequency even though w is altered. Therefore, to match with those invariable $\lambda_{0,e}$, different $\lambda_{0,m}$ of the fundamental magnetic SPs can be easily obtained by altering w instead of w'_G or p. The electric-SP modes of n = 4, 6, and 8 are found at $\lambda_{0,e}$ = 10.15, 9.38, and 8.76 μm, respectively. If the varied $f_{SP,m}$ approach those $f_{SP,e}$ individually, significant enhancement of the absorption is always observed, attributable to the strong EM-coupling effect between the magnetic and the electric SPs. By the way, the SP coupling can be applied to absorption-band broadening or splitting. Generally, the latter is accompanied by a phenomenon of EM-induced reflection or transparency.

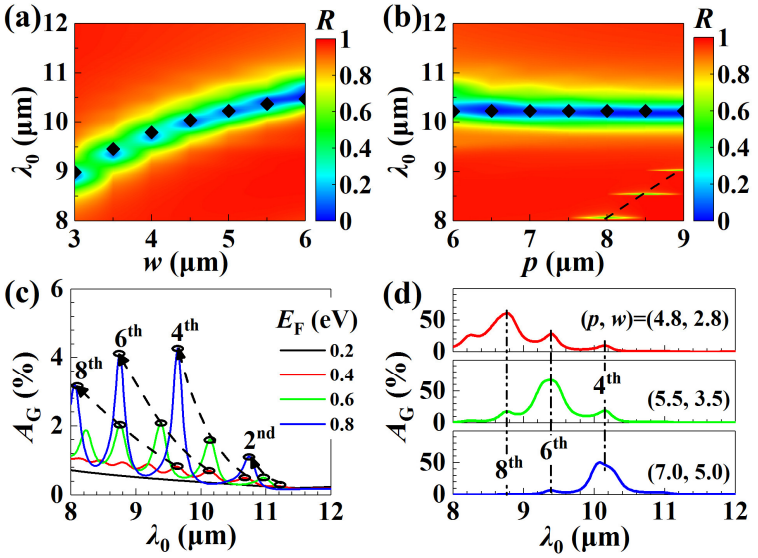

Fig. 3. At E_F = 0.4 eV, the device reflectance (R) contours: (a) dependence of w when the period of p = 7.0 μm is fixed; on the contrary, (b) dependence of p when the grating width of w = 5.0 μm is fixed. Dash line: the electric SPs along Air/Metal interface of the gratings; scattered symbol: calculated $\lambda_{0,m}$. Spectra in absorbance of the graphene (A_G): (c) at the different E_F and for the device in the structure of (p, w) = (3.0, 1.0), where the electric SPs in the different mode are solely involved in LWIR region; (d) at E_F = 0.6 eV and under the magnetic- and electric-SP coupling when the slotted-graphene width of w_G' = 2.0 μm is fixed. To approach $f_{SP,e}$ in the modes of n = 4, 6, and 8 individually, the various structures in (p, w) are selected to alter the fundamental $f_{SP,m}$.

In contrast, $f_{SP,e}$ can be determined by the F-P model of coherent SPPs in cavity modes. If the surface-wave-vector condition is satisfied, the graphene SPPs are supported to propagate along the Air/Graphene/Al_2O_3 interfaces, and their dispersion relation can be expressed as [36]:

$$\frac{1}{\sqrt{k_{SPP}^2 - k_0^2}} + \frac{\varepsilon_D}{\sqrt{k_{SPP}^2 - \varepsilon_D k_0^2}} = -\frac{i\sigma}{\omega\varepsilon_0}, \tag{6}$$

Optics EXPRESS

where $k_{SPP} = k'_{SPP} + ik''_{SPP}$ is the complex wave vector of graphene SPPs, and $k_0 = \omega/c$ is the vacuum wave vector. For $k'_{SPP} >> k_0$, Eq. (6) simplifies to:

$$k'_{SPP} \approx \frac{\varepsilon_0(1+\varepsilon_D)}{2}\frac{2\omega\sigma''}{\sigma'^2+\sigma''^2}. \tag{7}$$

In the model, F-P cavities of the interfaces are formed between the two neighboring gratings, and the coherent SPPs propagating in opposite directions along the interfaces are interfered. The well-known resonance condition is given by $k'_{SPP} = (n\pi - \Delta\varphi)/w'_G$, where $\Delta\varphi$ is the phase pickup upon grating edge reflection. To substitute the k'_{SPP} in Eq. (7), we obtain the electric-SP frequency

$$f_{SP,e} = \frac{1}{2\pi}\frac{n\pi-\Delta\varphi}{\varepsilon_0(1+\varepsilon_D)w'_G}\frac{\sigma'^2+\sigma''^2}{\sigma''};\ n = 2, 4, 6\ldots \tag{8}$$

As the antisymmetric odd modes are restrained, only even modes of the electric SPs are symmetric to be excited [to see Fig. 5(b)]. Different from $\Delta\varphi \approx \pi/4$ for the graphene ribbons within an open boundary [37,38], the phase is $\Delta\varphi \approx -3\pi/4$ for the graphene SPPs confined between conductive boundaries upon the grating edge reflection. It is due to the absence of tangential electric field at the boundary as the high conductivity of Au is used. As shown in Fig. 4, $\lambda_{0,e}$ calculated from Eq. (8) is also in good agreement with the simulated, especially for the mode of $n = 4$. Larger errors occurred in the other modes are probably resulted from: i) the mode dependence of the reflection phase in calculation; ii) effects of the metal inductance and the dielectric capacitance in simulation; in addition, iii) the longer SP wavelength ($\lambda_{SP} = 2\pi/k'_{SPP}$), the weaker confinement. The reflection phase for the lower-order mode may exhibit stronger $\lambda_{0,e}$-dependence than the higher-order modes.

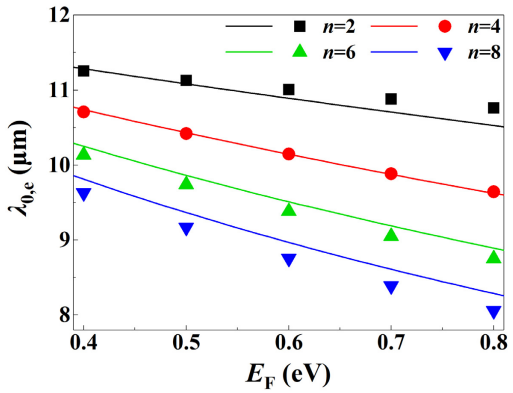

Fig. 4. For the device in the structure of (p, w) = (3.0, 1.0), E_F dependence of $\lambda_{0,e}$ in different mode. $\lambda_{0,e}$: calculated (in line); simulated (in symbol).

After the structural parameters are fixed, any deviation of $f_{SP,e}$ from $f_{SP,m}$ can be corrected by tuning the graphene Fermi energy. Figure 5(a) shows E_F dependence of the graphene absorption for the finally determined structure of (p, w) = (5.5, 3.5). As the magnetic SPs are solely involved in LWIR region, only one absorption peak is observable for the graphene at E_F = 0.2 eV, and the absorbance has a maximum of A_G = 25% at λ_0 = 9.50 μm. If the Fermi energy increases to E_F = 0.6 eV, the peak at λ_0 = 9.38 μm that corresponds to the electric-SP mode of n = 6 is significantly enhanced. Peak absorbance of the graphene is confirmed to exceed 67.2%, *i.e.*, an enhancement over 29-fold the absorbance of a suspended graphene (general 2.3%). In addition, with the ohmic dissipation of 12.3% from all the metals and the dielectric loss of 19.5%, the system of device has an absorbance close to A_{SYS} = 100%. If a

Optics EXPRESS

lossless dielectric is applied, it is anticipated that the graphene absorbance can be further boosted to 83.7%. However, other four peaks observed at λ_0 = 10.96, 10.15, 8.76, and 8.25 μm are much lower, and correspond to the electric-SP mode of n = 2, 4, 8, and 10, respectively. As illustrated in Fig. 5(b), the lower absorptions are attributable to the weaker electric-field intensities in the graphene; here, the distributions for the modes of n = 8 and 10 are not shown because their maximum intensities are close to the modes of n = 4 and 2, respectively. Detuning of the frequency results in the decrease of EM-coupling efficiency between the magnetic and the electric SPs. In addition, the standing-wave effect from the coherent interference of SPPs further restrains the energy from flowing between the two neighboring electric- or magnetic-SP elements.

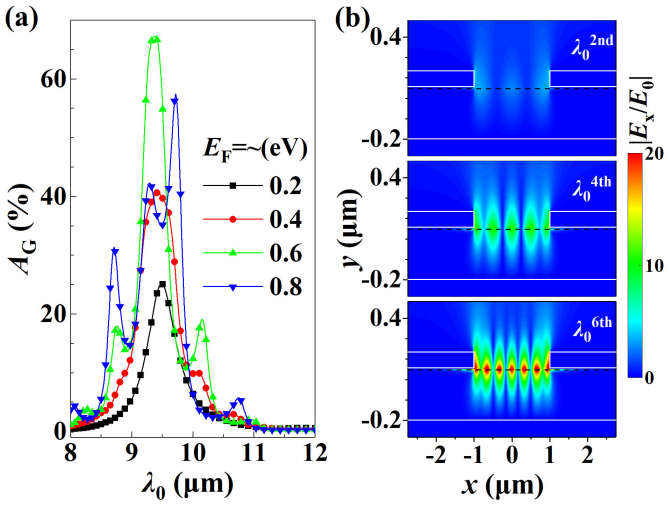

Fig. 5. (a) When (p, w) = (5.5, 3.5), absorbance spectra of the graphene (A_G) at different E_F. When E_F = 0.6 eV, three intense peaks, located at λ_0 = 10.15, 9.38, and 8.76 μm, correspond to the electric SPs in the modes of n = 4, 6, and 8, respectively. (b) At the three peaks, normalized field of $|\boldsymbol{E}_x|/|\boldsymbol{E}_0|$ along the x axis. Boundaries of the grating and bottom metal (in white solid line) and graphene (in black dash) are highlighted.

In case the carrier mobility is different, enhancing the graphene absorption still can be attained, and the center frequency is fixed when the Fermi energy keeps unchanged. Figure 6(a) shows the graphene absorbance dependence of the carrier mobility. There seems no difference in the maximum absorbance of the graphene between $\mu = 1 \times 10^3$ and 2×10^3 $cm^2V^{-1}s^{-1}$. As the mobility increases, the absorption peak slightly drops in height and width, while the frequency is always locked at λ_0 = 9.38 μm by fixing the Fermi energy at E_F = 0.6 eV. The maximum absorbance is reduced to 48.4% till $\mu = 1 \times 10^4$ $cm^2V^{-1}s^{-1}$. Since $E_F >> k_BT$, from Eqs. (1) and (7) it is straightforward to obtain [34]

$$k'_{SPP} \approx \frac{\pi\hbar^2\varepsilon_0(1+\varepsilon_D)}{e^2E_F}\omega^2, \tag{9}$$

indicating that the k'_{SPP} is μ-independent. If E_F>~0.2 eV, the optical phonon energy of graphene [34], ε'_G<<0, in the spectral regime of interest, and from Eqs. (1) and (3) the inductance thus can be expressed as

$$L_{e,G} \approx \gamma_1 \frac{w'_G}{l}\frac{\pi\hbar^2}{e^2E_F}. \tag{10}$$

Optics EXPRESS

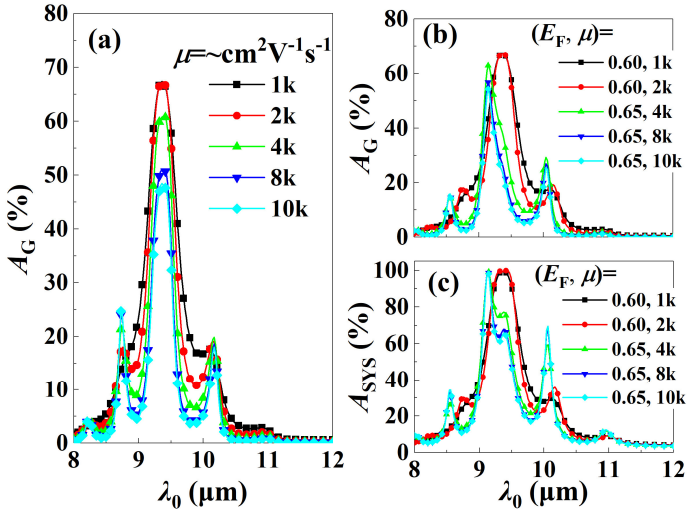

Fig. 6. The device is designed in the structure of (p, w) = (5.5, 3.5). The carrier mobility dependence of the absorbance spectra: for the graphene (A_G) (a) at E_F = 0.6 eV and (b) around E_F = 0.6 eV, as well as (c) for the system of device (A_{SYS}) around E_F = 0.6 eV.

Only if E_F<0.75 eV to satisfy $L_{e,M}$<<$L_{e,G}$, from Eqs. (4) and (5), $f_{SP,e}$ and $f_{SP,m}$ also become μ-independent. Figures 6(b) and 6(c) show how the absorption spectra change with the mobility and the Fermi energy. The graphene and the system absorbance can be further increased by fine tuning the Fermi energy to shift the center frequency of EM-induced reflection, which is more clearly observed for the higher mobility. At E_F = 0.65 eV, the graphene absorbance is increased to A_G = 54.3% for μ = 1 × 10^4 $cm^2V^{-1}s^{-1}$; especially, the device always can keep the system absorbance close to A_{SYS} = 100% even though the graphene exhibits the different mobility. To an absorber, the improvement is significant, too.

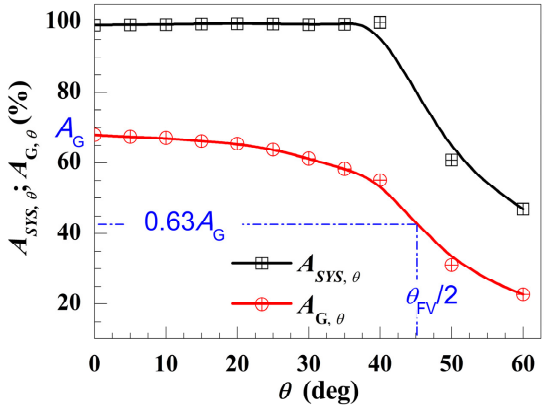

Fig. 7. For the device in the structure of (p, w)=(5.5, 3.5), the absorbance of graphene ($A_{G,\theta}$) and system ($A_{SYS,\theta}$) at λ_0=9.38 μm changes with the radiation incident angle (θ). The graphene: E_F=0.6 eV; μ=2×10^3 $cm^2V^{-1}s^{-1}$. The field angle is determined: at θ=θ_{FV}/2, the graphene absorbance is dropped by 0.37 times that at normal incident.

After the working wavelength is locked, the field angle of view can be determined for the device. Figure 7 shows the graphene and system absorptions at λ_0 = 9.38 μm dependence of the radiation incident angle (θ). Although the graphene absorbance decreases with the increasing angle, the system one keeps nearly unchanged when θ≤40°. From the decreasing absorbance of graphene, we determine the field angle up to θ_{FV} = 90°.

Optics EXPRESS

4. Conclusions

In summary, we have designed the graphene LWIR photodetector with a metasurface structure capable of significantly enhancing the optical absorption in the graphene. Peak absorbance of the graphene is confirmed to exceed 67.2%, and can be anticipated to reach 83.7% if a lossless dielectric is applied. With electric and magnetic resonances in matching frequencies, the absorption enhancement is attributed to the strong EM-coupling effect between the magnetic and the electric SPs, as well as the coherent interference of the graphene SPPs. In case of the graphene in different mobility, significantly enhancing the absorption always can be realized at the fixed frequency, due to the grating and the slot widths designed in the same order of magnitude, and the system absorbance keeps close to 100%. In addition to revealing the underlying coupling mechanism, the equivalent circuit method and the F-P model of coherent SPPs used in this work can also be used to accurately predict the wavelengths of magnetic and electric SPs. This study offers a new approach to design high-performance graphene photodetector and other relevant optoelectronic devices.

Funding

National Natural Science Foundation of China (NSFC) (Grant Nos. 61435004, 61675080, and 61735018); Fundamental Research Funds for the Central Universities (HUST: 2016YXMS021).

References

1. Q. Bao and K. P. Loh, "Graphene photonics, plasmonics, and broadband optoelectronic devices," ACS Nano **6**(5), 3677–3694 (2012).
2. F. Bonaccorso, Z. Sun, T. Hasan, and A. C. Ferrari, "Graphene photonics and optoelectronics," Nat. Photonics **4**(9), 611–622 (2010).
3. J. H. Chen, C. Jang, S. Xiao, M. Ishigami, and M. S. Fuhrer, "Intrinsic and extrinsic performance limits of graphene devices on SiO_2," Nat. Nanotechnol. **3**(4), 206–209 (2008).
4. P. Avouris, "Graphene: electronic and photonic properties and devices," Nano Lett. **10**(11), 4285–4294 (2010).
5. R. R. Nair, P. Blake, A. N. Grigorenko, K. S. Novoselov, T. J. Booth, T. Stauber, N. M. Peres, and A. K. Geim, "Fine structure constant defines visual transparency of graphene," Science **320**(5881), 1308 (2008).
6. F. J. García de Abajo, "Graphene plasmonics: challenges and opportunities," ACS Photonics **1**(3), 135–152 (2014).
7. T. Low and P. Avouris, "Graphene plasmonics for terahertz to mid-infrared applications," ACS Nano **8**(2), 1086–1101 (2014).
8. A. N. Grigorenko, M. Polini, and K. S. Novoselov, "Graphene plasmonics," Nat. Photonics **6**(11), 749–758 (2012).
9. S. Qu, C. Ma, and H. Liu, "Tunable graphene-based hybrid plasmonic modulators for subwavelength confinement," Sci. Rep. **7**(1), 5190 (2017).
10. X. Wang, C. Chen, L. Pan, and J. Wang, "A graphene-based Fabry-Pérot spectrometer in mid-infrared region," Sci. Rep. **6**(1), 32616 (2016).
11. L. Ju, B. Geng, J. Horng, C. Girit, M. Martin, Z. Hao, H. A. Bechtel, X. Liang, A. Zettl, Y. R. Shen, and F. Wang, "Graphene plasmonics for tunable terahertz metamaterials," Nat. Nanotechnol. **6**(10), 630–634 (2011).
12. S. Xia, X. Zhai, L. Wang, and S. Wen, "Plasmonically induced transparency in double-layered graphene nanoribbons," Photon. Res. **6**(7), 692–702 (2018).
13. N. Matthaiakakis, X. Yan, H. Mizuta, and M. D. B. Charlton, "Tuneable strong optical absorption in a graphene-insulator-metal hybrid plasmonic device," Sci. Rep. **7**(1), 7303 (2017).
14. B. Zhao and Z. M. Zhang, "Strong plasmonic coupling between graphene ribbon array and metal gratings," ACS Photonics **2**(11), 1611–1618 (2015).
15. S. X. Xia, X. Zhai, Y. Huang, J. Q. Liu, L. L. Wang, and S. C. Wen, "Multi-band perfect plasmonic absorptions using rectangular graphene gratings," Opt. Lett. **42**(15), 3052–3055 (2017).
16. L. Zhang, L. Tang, W. Wei, X. Cheng, W. Wang, and H. Zhang, "Enhanced near-infrared absorption in graphene with multilayer metal-dielectric-metal nanostructure," Opt. Express **24**(18), 20002–20009 (2016).
17. B. Zhao, J. M. Zhao, and Z. M. Zhang, "Enhancement of near-infrared absorption in graphene with metal gratings," Appl. Phys. Lett. **105**(3), 031905 (2014).
18. Y. S. Fan, C. C. Guo, Z. H. Zhu, W. Xu, F. Wu, X. D. Yuan, and S. Q. Qin, "Monolayer-graphene-based perfect absorption structures in the near infrared," Opt. Express **25**(12), 13079–13086 (2017).
19. X. Jiang, T. Wang, S. Xiao, X. Yan, and L. Cheng, "Tunable ultra-high-efficiency light absorption of monolayer graphene using critical coupling with guided resonance," Opt. Express **25**(22), 27028–27036 (2017).

Optics EXPRESS

20. Y. Cai, J. Zhu, Q. H. Liu, T. Lin, J. Zhou, L. Ye, and Z. Cai, "Enhanced spatial near-infrared modulation of graphene-loaded perfect absorbers using plasmonic nanoslits," Opt. Express **23**(25), 32318–32328 (2015).
21. Y. Zhang, T. Li, Q. Chen, H. Zhang, J. F. O'Hara, E. Abele, A. J. Taylor, H. T. Chen, and A. K. Azad, "Independently tunable dual-band perfect absorber based on graphene at mid-infrared frequencies," Sci. Rep. **5**(1), 18463 (2016).
22. A. Akhavan, H. Ghafoorifard, S. Abdolhosseini, and H. Habibiyan, "Plasmon-induced transparency based on a triangle cavity coupled with an ellipse-ring resonator," Appl. Opt. **56**(34), 9556–9563 (2017).
23. Y. Cai, J. Zhu, and Q. Liu, "Tunable enhanced optical absorption of graphene using plasmonic perfect absorbers," Appl. Phys. Lett. **106**(4), 043105 (2015).
24. M. Freitag, T. Low, L. Martin-Moreno, W. Zhu, F. Guinea, and P. Avouris, "Substrate-sensitive mid-infrared photoresponse in graphene," ACS Nano **8**(8), 8350–8356 (2014).
25. B. Deng, Q. Guo, C. Li, H. Wang, X. Ling, D. B. Farmer, S. J. Han, J. Kong, and F. Xia, "Coupling-enhanced broadband mid-infrared light absorption in graphene plasmonic nanostructures," ACS Nano **10**(12), 11172–11178 (2016).
26. U. Sassi, R. Parret, S. Nanot, M. Bruna, S. Borini, D. De Fazio, Z. Zhao, E. Lidorikis, F. H. Koppens, A. C. Ferrari, and A. Colli, "Graphene-based mid-infrared room-temperature pyroelectric bolometers with ultrahigh temperature coefficient of resistance," Nat. Commun. **8**, 14311 (2017).
27. Q. Guo, R. Yu, C. Li, S. Yuan, B. Deng, F. J. García de Abajo, and F. Xia, "Efficient electrical detection of mid-infrared graphene plasmons at room temperature," Nat. Mater. **17**(11), 986–992 (2018).
28. E. D. Palik, *Handbook of Optical Constants of Solids* (Academic, 1991).
29. L. A. Falkovsky, "Optical properties of graphene," J. Phys. Conf. Ser. **129**, 012004 (2008).
30. Y. Yao, M. A. Kats, P. Genevet, N. Yu, Y. Song, J. Kong, and F. Capasso, "Broad electrical tuning of graphene-loaded plasmonic antennas," Nano Lett. **13**(3), 1257–1264 (2013).
31. J. Zhou, L. Zhang, G. Tuttle, T. Koschny, and C. M. Soukoulis, "Negative index materials using simple short wire pairs," Phys. Rev. B Condens. Matter Mater. Phys. **73**(4), 041101 (2006).
32. X. L. Liu, B. Zhao, and Z. M. Zhang, "Blocking-assisted infrared transmission of subwavelength metallic gratings by graphene," J. Opt. **17**(3), 035004 (2015).
33. A. Sakurai, B. Zhao, and Z. M. Zhang, "Resonant frequency and bandwidth of metamaterial emitters and absorbers predicted by an RLC circuit model," J. Quant. Spectrosc. Radiat. Transf. **149**, 33–40 (2014).
34. V. D. Lam, J. B. Kim, S. J. Lee, Y. P. Lee, and J. Y. Rhee, "Dependence of the magnetic-resonance frequency on the cut-wire width of cut-wire pair medium," Opt. Express **15**(25), 16651–16656 (2007).
35. B. J. Lee, L. P. Wang, and Z. M. Zhang, "Coherent thermal emission by excitation of magnetic polaritons between periodic strips and a metallic film," Opt. Express **16**(15), 11328–11336 (2008).
36. M. Jablan, H. Buljan, and M. Soljačić, "Plasmonics in graphene at infrared frequencies," Phys. Rev. B Condens. Matter Mater. Phys. **80**(24), 245435 (2009).
37. L. Du, D. Tang, and X. Yuan, "Edge-reflection phase directed plasmonic resonances on graphene nano-structures," Opt. Express **22**(19), 22689–22698 (2014).
38. A. Y. Nikitin, T. Low, and L. Martin-Moreno, "Anomalous reflection phase of graphene plasmons and its influence on resonators," Phys. Rev. B Condens. Matter Mater. Phys. **90**(4), 041407 (2014).